

Research Paper

Application of CFD-DEM to investigate seepage characteristics of landslide dam materials

Zhen-Ming Shi^{a,b,c}, Hong-Chao Zheng^{a,b}, Song-Bo Yu^{a,b,*}, Ming Peng^{a,b}, Tao Jiang^d

^a Key Laboratory of Geotechnical and Underground Engineering of Ministry of Education, Department of Geotechnical Engineering, Tongji University, Shanghai 200092, China

^b Department of Geotechnical Engineering, College of Civil Engineering, Tongji University, Shanghai 200092, China

^c Collaborative Innovation Center of Geohazard Prevention (CICGP), Chengdu, Sichuan 610059, China

^d Department of Underground Structures and Geotechnical Engineering, Shanghai Underground Space Engineering Design and Research Institute, Arcplus Group PLC, Shanghai, China

ARTICLE INFO

Keywords:

Landslide dam
CFD-DEM
Seepage failure
Flowing soil
Piping

ABSTRACT

A coupled computational fluid dynamics and discrete element method was presented to quantitatively investigate the seepage characteristics of fine and coarse materials relevant to landslide dam. The numerical model was verified by comparing the calculated seepage parameters, critical hydraulic gradient and failure mode with the corresponding tests. The microcosmic mechanisms of the seepage failure were studied by considering seepage field, force chain, and particle trajectory. The failure mode of fine-grained soils was flowing soil because the effective stress was close to zero. However, for coarse-grained soils, the failure mode was piping that resulted from the presence of some effective stress.

1. Introduction

Landslide dams are formed when a river is blocked by mass movements such as a rock avalanche, landslide, or debris flow triggered by an earthquake, heavy rainfall, or other factors [1,2]. According to Costa [3] and Shi [4], the failure modes of landslide dams mainly consist of overtopping and seepage failure (flowing soil and piping). Flowing soil occurs where the uplift force of the downstream dam exceeds the buoyant weight with a rapid increase in the upstream water level [5]. Piping is caused by migration of small particles to free exits or into coarse openings, such as large pores in gravels or cobbles [6]. The grain compositions of the dam materials are continually changed by permeation, and this undermines the long-term stability and longevity of the landslide dams [7]. People's lives and property in the downstream areas are seriously threatened by severe dam-breaching floods and the sediments deposited in the process [8,9]. Therefore, it is necessary to further study the seepage characteristics of landslide dam materials.

Field tests, laboratory tests, and numerical simulations are the main research approaches to study the seepage characteristics of landslide dams. Currently, there are only a few field tests such as pumping tests and water injection tests used to obtain hydraulic conductivity. For example, tests were carried out on the Xiaonanhai barrier dam [10] and the Tangjiashan landslide dam [11]. It is difficult to conduct an onsite

investigation of the seepage stability of landslide dams because of limitation related to by personnel security, poor geological environment, and short longevity of the landslide dams.

Laboratory test is the conventional method used to investigate the seepage characteristics of geotechnical materials from the macro perspective by measuring the hydraulic conductivity and critical hydraulic gradient [12–14]. A large amount of data has been accumulated from such experiments [15–20] to investigate the failure mechanism in flowing soil and piping as well as to assess the seepage stability. Nevertheless, there is still a lack of understanding of the physical failure process for different types of soils because of the absence of information on the particle trajectory and stress variables.

Conventional numerical approaches based on continuum theories of porous media, such as the Biot theory, consider the interaction between pore water and particles in a phenomenological manner. However, they cannot offer micro information at the particle level regarding the fluid-particle interaction [21]. The DEM (discrete element method) [22], based on the discontinuous media theory, has an outstanding advantage of simulating the interactions among particles. Muir [23] employed a two-dimensional DEM to simulate the progressively narrowing granular composition of the soil in the internal erosion process by removing the small particles. Hicher [24] applied the DEM to analyze the mechanical behavior of soils subjected to internal erosion by increasing the void

* Corresponding author at: Key Laboratory of Geotechnical and Underground Engineering of Ministry of Education, Department of Geotechnical Engineering, Tongji University, Shanghai 200092, China.

E-mail address: yusongbo@tongji.edu.cn (S.-B. Yu).

<https://doi.org/10.1016/j.compgeo.2018.04.020>

Received 9 November 2017; Received in revised form 21 April 2018; Accepted 22 April 2018

Available online 26 April 2018

0266-352X/ © 2018 Elsevier Ltd. All rights reserved.

ratio of the granular assembly. A description of the development process of seepage failure is not obtained merely by using the DEM without considering pore water, which has transportation effects on the particles. Hence, a coupled CFD-DEM (computational fluid dynamics and discrete element method) analysis method provides an innovative approach to explore the seepage characteristics and failure modes of soil materials. This model uses a CFD module and a DEM module to manage the motion state of the pore water and solid particles, respectively, and exchanges proper interaction forces between the two modules. This model has been successfully applied to study some geotechnical engineering issues. For example, Suzuki [25] and Chen [26] employed the CFD-DEM model to verify the dissipation law of excess pore water pressure and proposed three parameters that affect computational convergence: the viscous damping coefficient, the time step of the solution processes for the fluid and solid particles, and the number of solid particles per unit volume. Zhao [21] applied the model to investigate the characteristics of sand heaps formed in water through hopper flow, while Jing [27] simulated the Couette flow of a suspension and evaluated the nonlinear velocity profiles with different porous spheres. With regard to seepage failure, limited computational studies have been performed. Zhao [28] used this method to conduct qualitative research on the mechanism of piping in narrow-graded sandy soils. However, the CFD-DEM model has been seldom applied to quantitatively investigate the seepage characteristics of wide-graded soils like landslide dam materials, because of limitations of computational convergence. In addition, the seepage failure mechanism has not been adequately understood yet.

The objective of this study is to simulate a series of seepage tests on fine-grained and coarse-grained soils (landslide dam materials) with various dry densities by using the coupled CFD-DEM model to reveal the seepage failure mechanism from the microscopic view. The numerical method was verified with a laboratory test for the calculated seepage parameters, critical hydraulic gradient, and failure mode.

2. Methodology of the CFD-DEM model for seepage analysis

The CFD-DEM model consists of DEM and CFD modules. The numerical solution procedures, derivation of the governing equation, and the modified method of computational convergence are described in detail in the following sections.

2.1. Numerical solution procedures for the CFD-DEM model

Instead of solving the DEM and CFD modules concurrently, an iterative procedure is adopted as shown in Fig. 1. Under a given constant hydraulic gradient, the DEM solver is first used to renew the particle position, and then, the resultant interaction force f_{int} and porosity n are updated and transported to the CFD module. Under pressure boundary conditions, the flow velocity \mathbf{v} and pressure gradient ∇p are solved by Navier–Stokes equations, and then, a new interaction force f_{int} and porosity n are obtained and transmitted back to the DEM module for the next time step. The iterations continue until the flow velocity \mathbf{v} of the pore water reaches a steady state value.

2.2. Governing equations for the CFD-DEM model

The motion of the particle assembly in the DEM module is governed by Newton's equation,

$$m \frac{d\mathbf{u}}{dt} = (\mathbf{f}_g + \mathbf{f}_{int} + \mathbf{f}_c) \quad (1)$$

where m is the mass, \mathbf{u} is the velocity of the particle, and t is the time. \mathbf{f}_g is gravity force, \mathbf{f}_{int} is the particle–fluid interaction force, and \mathbf{f}_c is the contact forces from proximal particles.

The governing equations for the CFD module are the averaged Navier–Stokes equations [29], including the conservation equation of

mass and momentum, which are given below:

$$\frac{\partial n}{\partial t} = -(\nabla \cdot n\mathbf{v}) \quad (2)$$

$$\frac{\partial(n\mathbf{v})}{\partial t} = -(\nabla \cdot n\mathbf{v}\mathbf{v}) - \frac{n}{\rho_f} \nabla p - \frac{n}{\rho_f} \nabla \cdot \boldsymbol{\tau} - \frac{\mathbf{f}_{int}}{\rho_f} + n\mathbf{g} \quad (3)$$

where ρ_f is the density of pore water, \mathbf{v} is the flow velocity of a fluid cell, n is porosity, and \mathbf{g} is the gravity acceleration. $\boldsymbol{\tau}$ is the viscous stress tensor for Newtonian fluids.

The particle–fluid interaction force \mathbf{f}_{int} consists of a buoyancy force \mathbf{f}_b and drag force \mathbf{f}_d . There have been some empirical regression equations used to calculate the drag force \mathbf{f}_d , of which the following equation of Tsuji [30] is widely used. For porosity [31] $n \leq 0.8$:

$$\mathbf{f}_d = 150 \frac{1-n}{d_p^2} \eta (\mathbf{v} - \bar{\mathbf{u}}) V_i + 1.75 \frac{1}{d_p} \rho_f |\mathbf{v} - \bar{\mathbf{u}}| (\mathbf{v} - \bar{\mathbf{u}}) V_i \quad (4)$$

where V_i is the volume of the solid particles in the fluid cell i , \bar{d}_p is the average grain diameter in a fluid cell, and η is the viscosity coefficient of pore water. With regard to the migration of solid particles, $(\mathbf{v} - \bar{\mathbf{u}})$ represents the relative velocity of pore water against the particles.

The first term on the right side of Eq. (4) is in accordance with Darcy's law, wherein this term is directly proportional to $(\mathbf{v} - \bar{\mathbf{u}})$, and it is principally applied in a laminar flow. The second term in the equation is proportional to $(\mathbf{v} - \bar{\mathbf{u}})^2$ and has a significant influence on turbulent flow. The first and second terms correspond to viscous and inertial force components of \mathbf{f}_d , respectively [32]. There may be a great difference in the forces for different types of soil materials, and this is discussed in the next section.

2.3. Cluster element generation for computational convergence

It is very difficult to compute when the size ratio of fluid cell to particle diameter is less than four, because of significant fluctuations in porosity n [27]. In this study, the cluster element generation method is adopted to ensure computational convergence and accuracy when a large particle is replaced by dozens of tightly bonded small particles at its initial position [33]. The cluster element interacts with the neighboring particles and pore water in the form of an entire particle, and thus the time consumed for calculation will not increase.

The main procedure of cluster element generation is as follows (Fig. 2): (a) first, search for the target particles and record the particle information such as coordinates and radius, (b) delete the target particle, (c) generate the main particle at the original position of the target particle, and (d) finally, generate tangent particles around the main particle with random phase angles and bond them with each other using the contact_bond model.

3. Experimental work on landslide dam materials

The seepage tests on landslide dam materials are briefly introduced in this section. The tests are conducted to verify the numerical simulation results obtained with the CFD-DEM model, which is covered in the next section.

3.1. Specimen selection

Tangjiashan landslide dam was triggered by the M_w 7.9 Wenchuan earthquake in the Longmenshan Fault zone in China; the dam has a height of 82 m and a reservoir capacity of $3.16 \times 10^8 \text{ m}^3$ [34]. Several centralized soakage zones were developed on the downstream side of the dam, compelling more than 200,000 people to evacuate urgently. The grain composition of the specimens in the laboratory test was based on the Tangjiashan landslide dam materials, as shown in Fig. 3 [35]. Two typical grading curves were derived, one for fine-grained soils indicated by the thick solid line and the other for coarse-grained soils

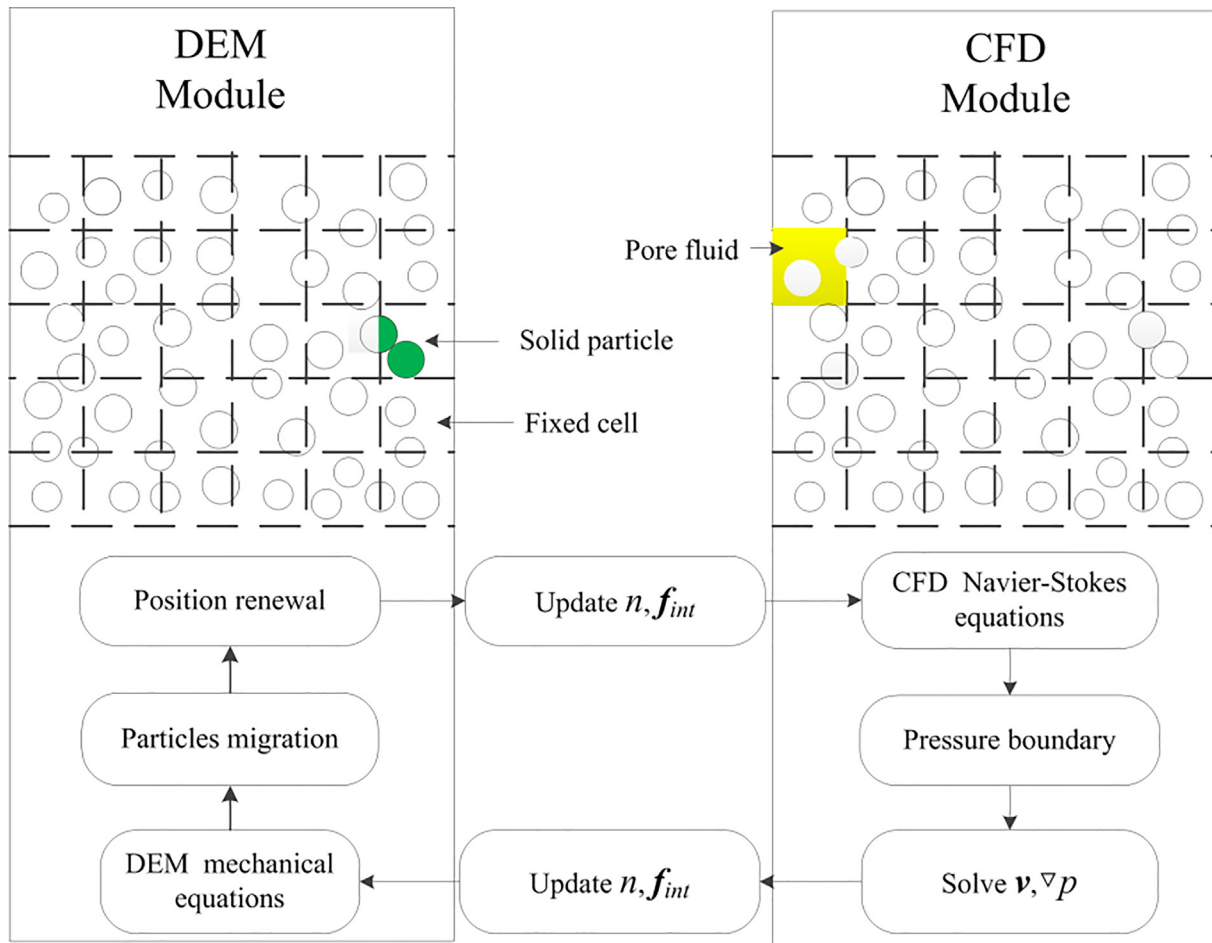


Fig. 1. Framework of CFD and DEM model coupling.

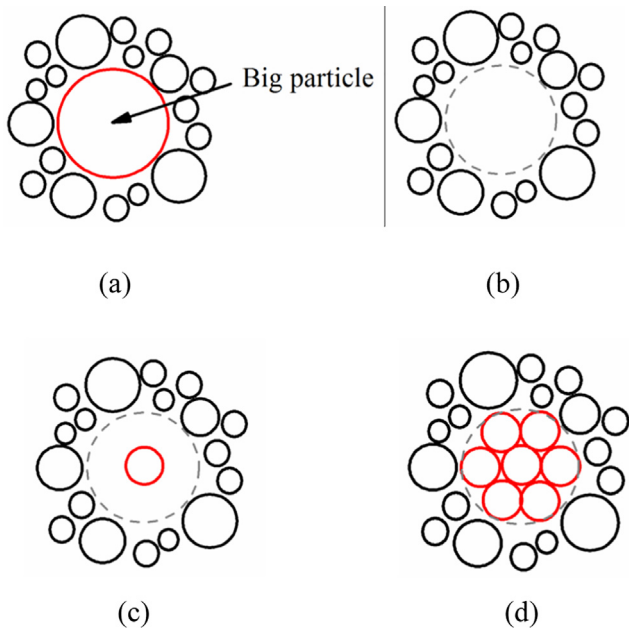


Fig. 2. Cluster element generation procedure.

indicated by the thick dashed line. The two soil types were defined according to the dam materials and were different from the standard of conventional engineering classification of soils. On the basis of drill-hole data [35,36], four values of dry densities were selected as 1.78,

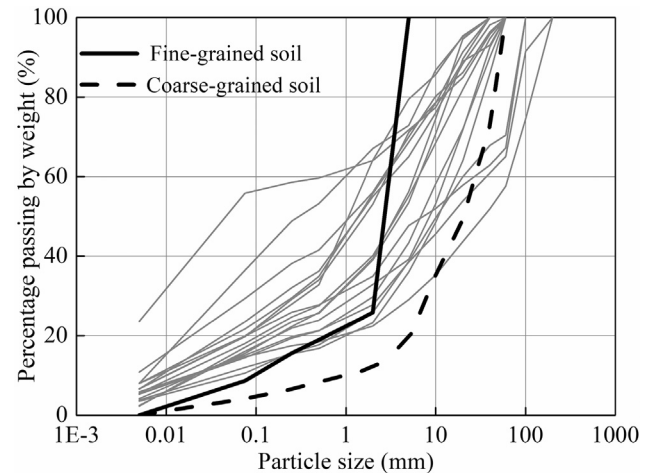


Fig. 3. Grading curves of Tangjiashan landslide dam.

1.82, 1.86, and 1.90 g/cm³ for fine-grained and coarse-grained soils. The serial numbers for the fine-grained soil specimens with these four densities were F1, F2, F3, and F4, and those for the coarse-grained soil specimens were C1, C2, C3, and C4, respectively.

3.2. Experimental device and operational procedure

The largest gravel in the coarse-grained soils, which has a grain diameter of 40 mm, will have a scale effect on the current seepage

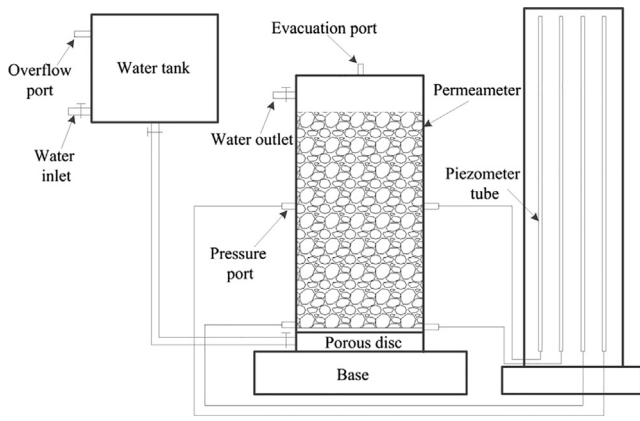


Fig. 4. Schematic representation of the experimental apparatus of seepage test.

meter with an inner diameter of less than 100 mm. If many small grains are present in the fine-grained soils, it is difficult to achieve a high level of saturation in the specimens when the conventional saturation method of using a water head is employed. Considering the above-mentioned factors, a modified seepage facility consisting of a permeameter, a water supply equipment, a measurement device, and a suction pump was developed based on the traditional seepage meter, as shown in Fig. 4. The material of the sidewall of the permeameter was organic glass, and thus, the seepage development process could be observed. The inner diameter of the permeameter was 300 mm, which is greater than five times the size of the maximum grain, and free from the size effect of large grains. The height of the device was 600 mm, and the aspect ratio met the standard for the soil test method. The required hydraulic gradient could be obtained by changing the height of the water tank in which water was supplied by a water pump. The two pairs of piezometer tubes switched by the tongs were installed symmetrically on the sidewall to measure the permeability gradient accurately. The distance between the upper and lower pressure inlets was 300 mm, and the distance between the lower pressure inlet and base was 50 mm. To attain saturation rapidly, a vacuum air pump was installed on the sealed cover plate located on the roof of the permeameter. Vertical flow was adopted in the specimens, and on the top of this, there was a free overflow surface.

Before the test, vaseline was smeared on the internal face of the permeameter to prevent leakage along the sidewall. The major steps are as follows.

- (1) Specimen preparation and saturation: The soil materials for the specimens were prepared based on the grain composition of fine-grained and coarse-grained soils, and they were filled into the permeameter in three uniform layers. After the specimen was compacted to the given height, it was immersed in water and subjected to vacuum saturation for more than 2 h.
- (2) Hydraulic gradient application: Based on the variation in the seepage velocity and specimen deformation, the interval time for the hydraulic gradient was determined to be 30 min for coarse-grained soils and 60 min for fine-grained soils. Approximately 10 data points were needed, considering the limited time available, so that the variation in the hydraulic gradient was in the range of 0.05–0.3 for fine-grained soils, and 0.05–0.1 for coarse-grained soils.
- (3) Date recording: When the seepage process was steady, the water levels in the two pairs of piezometer tubes were recorded by the scale plate, and the seepage quantity was sampled three times using the measuring cylinder with a time interval of 5 min. The test was terminated when the seepage quantity increased continually or an apparent seepage failure occurred.
- (4) Data processing: The seepage velocity v of the specimen and corresponding hydraulic gradient i were calculated, and the curve showing the relationship between i and v was mapped.

3.3. Results of the laboratory test

The seepage failure of specimens F1, F2, F3, and F4 was flowing soil. With the increase in i , some small particles jumped up and down on the top surface of the specimen, but no significant change appeared on the flank. Several horizontal fissures were seen on the top and bottom of the specimen at the critical failure state. Then, the seepage quantity increased suddenly, and the hydraulic gradient i dropped automatically, resulting in failure due to flowing soil. The seepage failure of specimens C1, C2, C3, and C4 was piping. Taking C1 as an example (Fig. 5), it was observed that the small particles with a grain diameter smaller than 0.5 mm migrated upward slowly when i was 0.12. The pore water changed from a milky white fluid to a transparent fluid; this was followed by the loss of small particles. When i was 0.28, the particles in the range of 0.5–2 mm started to float, leading to gradual linking of local pores in the specimen. Subsequently, the particles in the range of 2–10 mm were carried away along the local conduits when i was 0.49. At the critical failure state, several gushing springs developed on the top surface of the specimen, and an entire seepage passage from top to bottom was apparent on the sidewall.

The $i - v$ curves for the fine-grained and coarse-grained soils are

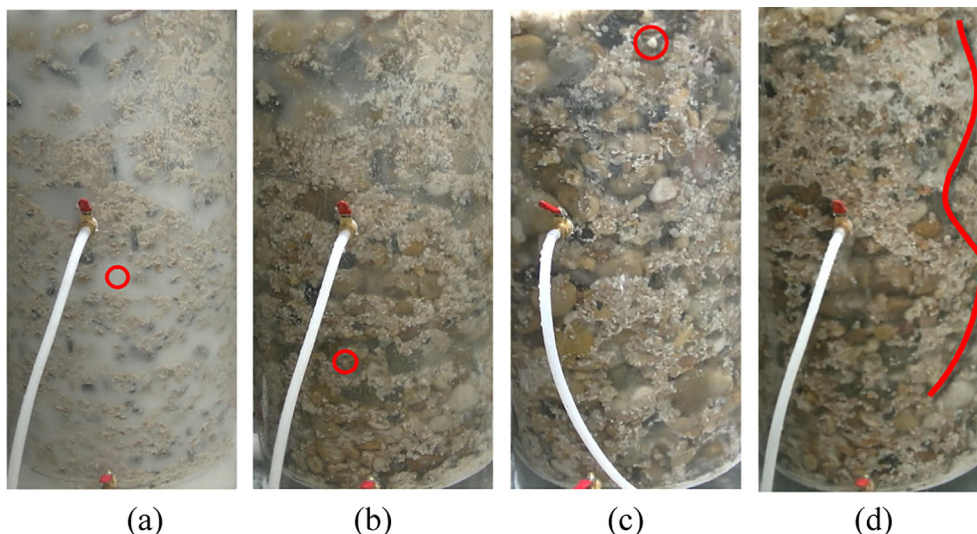


Fig. 5. Development process of seepage failure of C1: (a) $i = 0.12$ (b) $i = 0.28$ (c) $i = 0.49$ (d) $i = 0.82$ (piping).

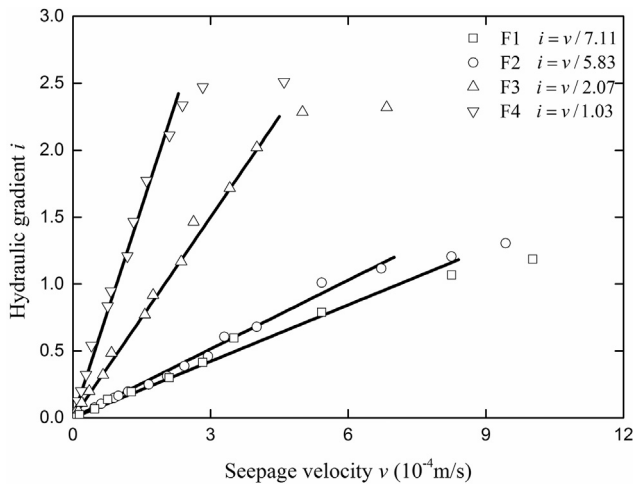


Fig. 6. The relationship $i - v$ of seepage test for fine-grained soils.

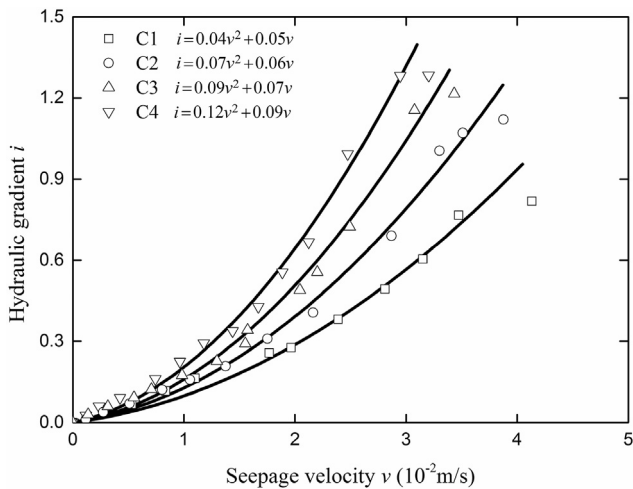


Fig. 7. The relationship $i - v$ of seepage test for coarse-grained soils.

shown in Figs. 6 and 7 respectively. The curves presented a linear and nonlinear relationship for the fine-grained and coarse-grained soils, respectively. The pore water in the fine-grained soils had a low seepage velocity (10^{-4} m/s), and it was linear Darcy flow. However, the pore

water in the coarse-grained soils was turbulent, with a high seepage velocity (10^{-2} m/s); therefore, it changed to become non-Darcy flow. In addition, critical hydraulic gradient, i.e., permeability resistance, was enhanced with the increasing dry density, due to a smaller porosity. Owing to the absence of micro information, the detailed seepage failure mechanism could be explored by incorporating the data of the CFD-DEM numerical simulation in the next section.

4. CFD-DEM research on seepage characteristics of landslide dam materials

The seepage tests on fine-grained and coarse-grained soils with various dry densities were simulated. First, the reliability and accuracy of the CFD-DEM model was validated by performing a comparison with the results of the laboratory test. Then, the seepage failure mechanism was revealed based on the micro information on seepage field, force chain, particle trajectory, and coordination number.

4.1. Model setup and numerical simulation

The numerical model was developed in four main steps: wall generation, particle and cluster element generation, compaction and pressure release, and point wall and fluid cell generation.

- (1) Wall generation: Four orthogonal walls were generated with an aspect ratio of 2, based on the standard for the soil test method, as shown in Fig. 8(a). Like the laboratory test, the wall width, B should be greater than five times the largest grain diameter, and the number of particles should also be optimized to save calculation time. Hence, the model dimensions were determined as $15 \text{ mm} \times 30 \text{ mm}$ for the fine-grained soils and $200 \text{ mm} \times 400 \text{ mm}$ for the coarse-grained soils.
- (2) Particle and cluster element generation: Particle assembly with unit thickness was obtained using the particle generator in the software Particle Flow Code [37] in four uniform layers according to the grain size distribution obtained in the laboratory test. The details are presented in Table 1. To ensure calculation convergence, the particles with a grain diameter smaller than 0.25 mm in the fine-grained soils and 5 mm in the coarse-grained soils were made equivalent to those with grain diameters of 0.15 mm and 3 mm, respectively, as recommended in current specification of soil test [38]. The cluster replacement program was then executed by which the large particles (2 mm) were substituted with 7 small particles (0.67 mm) in the fine-grained soils, and the large particles (with

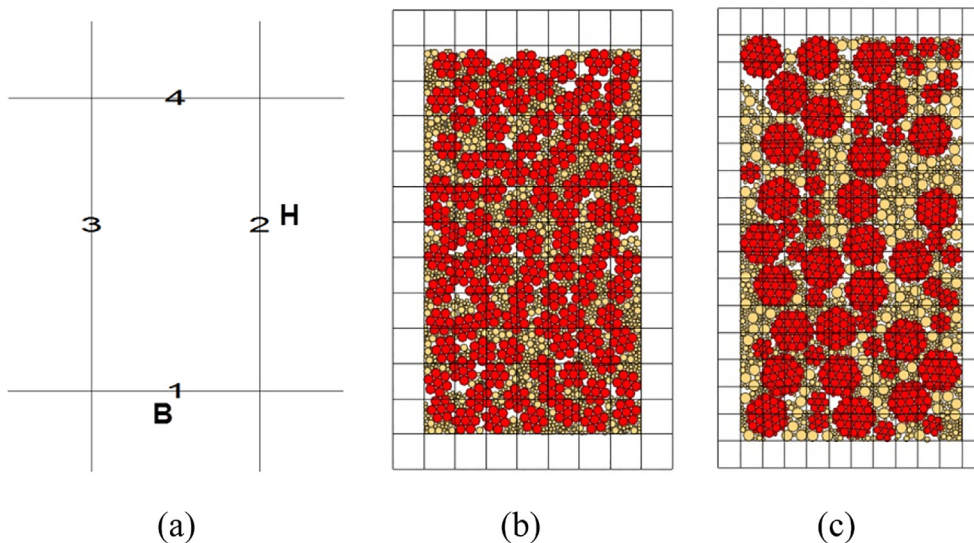


Fig. 8. Model setup: (a) wall generation (b) fine-grained soils (c) coarse-grained soils.

Table 1
Distributions of particle sizes in the numerical model.

	DIAMETER (mm)	2	0.5	0.25	0.15	
Fine-grained soil	Weight percentage (%)	74.17 (cluster)	6.88	3.36	5.59	
	Diameter (mm)	40	20	10	5	3
Coarse-grained soil	Weight percentage (%)	50.79 (cluster)	13.95 (cluster)	16.26	7.15	11.85

sizes of 40 mm and 20 mm) were replaced with 31 particles (19 particles of size 8 mm, and 12 particles of size 3.33 mm) and 7 particles (6.67 mm) in the coarse-grained soils. In Fig. 8(b) and (c), the red and yellow particles represent the cluster elements and the normal particles, respectively.

- (3) Compaction and pressure release: The top wall moved downward at a constant speed 0.05 mm/s until the desired dry density was achieved and the other walls remained static. After completion of the vertical movement of the top wall under the control of a numerical servo-mechanism, the contact force between the top wall and the particle assembly was released. Then, the top wall was removed.
- (4) Point wall and fluid cell generation: The bottom wall was replaced by a set of point walls with an interval of minimum grain diameter in order to form a bottom filter boundary. To ensure computational convergence, each fluid cell should contain dozens of particles. Hence, 7×11 cells were set up for the fine-grained soils and 10×15 for coarse-grained soils, as shown in Fig. 8(b) and (c), respectively. The physical parameters of the numerical model are presented in Table 2, and the material parameters that mainly referred to Li [39] are presented in Table 3.

The actual velocity v_{ij} and the porosity n in the fluid cell were recorded simultaneously during the calculation process. The superficial velocity v^0 was then obtained by multiplying v_{ij} and the corresponding n , as given in the following equation.

$$v^0 = \frac{\sum_{i=1}^k \sum_{j=1}^m v_{ij} n_{ij}}{k \times m} \quad (5)$$

where k and m were the row and column numbers, respectively, in the flow field.

4.2. Numerical results for fine-grained soils

The variation in the hydraulic gradient i was 0.3 in F1 and F2 and 0.4 in F3 and F4, but it reduced to 0.1 when v^0 could no longer remain stable. The critical gradient i_c was calculated by averaging the value of i when v^0 just fluctuated and the former one when v^0 was steady.

Table 2
Physical parameters of the numerical model.

Grain composition	Model size (mm × mm)	Fluid cell	Abbreviation	Compactness (g/cm ³)	Particle number
Fine-grained soil	15 × 30	7 × 11	F1	1.78	2246
			F2	1.82	2293
			F3	1.86	2346
			F4	1.90	2405
Coarse-grained soil	200 × 400	10 × 15	C1	1.78	2286
			C2	1.82	2337
			C3	1.86	2411
			C4	1.90	2489

Table 3
Material parameters of the numerical model.

Material parameters	Value
Grain density (g/cm ³)	2.65
Fluid density (g/cm ³)	1.0
Fluid viscous coefficient (Pa s)	0.001
Interparticle friction coefficient	0.7
Interparticle normal stiffness (N/m)	1×10^8
Interparticle shear stiffness (N/m)	5×10^7
Wall friction coefficient	0.3
Wall normal stiffness (N/m)	1×10^8
Wall shear stiffness (N/m)	1×10^8
Time step (DEM) (s)	2×10^{-7}
Time step (CFD) (s)	2×10^{-5}

4.2.1. Verification of the numerical model

The superficial velocity v^0 changed with the timestep (DEM) in the case of fine-grained soils with various dry densities, as shown in Fig. 9. When a hydraulic gradient i was applied instantaneously, the particle assembly adjusted its position because of the effect of buoyancy and drag force, which resulted in significant fluctuations in v^0 . Subsequently, the pore water flow reached a steady state, and v^0 was the ultimate superficial velocity v corresponding to the applied value of i . However, v^0 could not remain stable when the applied i was larger than the critical gradient i_c . The computing time for each i on a 4-core Intel CPU (4.0 GHz) desktop computer was more than three days.

The $i - v$ curve showed a direct proportional relationship for the fine-grained soils, as shown in Fig. 10, which was similar to the results of the laboratory tests shown in Fig. 6. The reciprocal of the slope of the straight line is the permeability coefficient k when the $i - v$ curve is fitted with the linear function. The goodness of fit R^2 of the regression straight line was greater than 0.9; this indicated a high level of conformance to Darcy's law, which is given by the following:

$$i = v/k \quad (6)$$

The migration rate of pore water was low, and the Reynolds number ($Re = \frac{\rho_f d_p u}{\eta}$) was small (the largest value was less than 2), resulting in the pore water remaining in the laminar flow state. The drag force f_d of the pore water against the particles was small, and it was mainly dominated by the viscous force, as given in Eq. (4). Thus, the relationship of $i - v$ was conformed with Darcy's law.

Flowing soil appeared in specimens F1, F2, F3, and F4, which was in accordance with the corresponding seepage tests. The values of k and i_c , listed in Table 4 were very close to those obtained from the laboratory tests. These verified the rationality of the application of the CFD-DEM model to investigate the seepage characteristics of the fine-grained soils.

4.2.2. Micro analysis of seepage failure for fine-grained soils

Typical model diagrams, seepage fields, corresponding force chains, particle trajectory, and coordination number were recorded to investigate the development process of flowing soil from micro perspective. Taking F1 as an example, the details are discussed as follows.

From the model diagram, the specimen was colored uniformly in four layers to clearly observe the relative movement of interlaminar particles (Table 5). The specimen showed a small variation during the entire seepage process. At the critical failure state ($i = 1.4$), the small particles on top of the specimen continually tumbled, bounced, and collided with the adjacent large particles. The entire particle assembly floated upward after a strip of horizontal fissure appeared; this was also the case with the laboratory test.

From the seepage field, the orientation and length of the arrows represented the direction and relative value of the seepage velocity in the fluid cell, respectively (Table 5). The value of v^0 increased with i , and the direction did not change. At the failure stage, the particles migrated between the fluid cells, leading to large variations in porosity

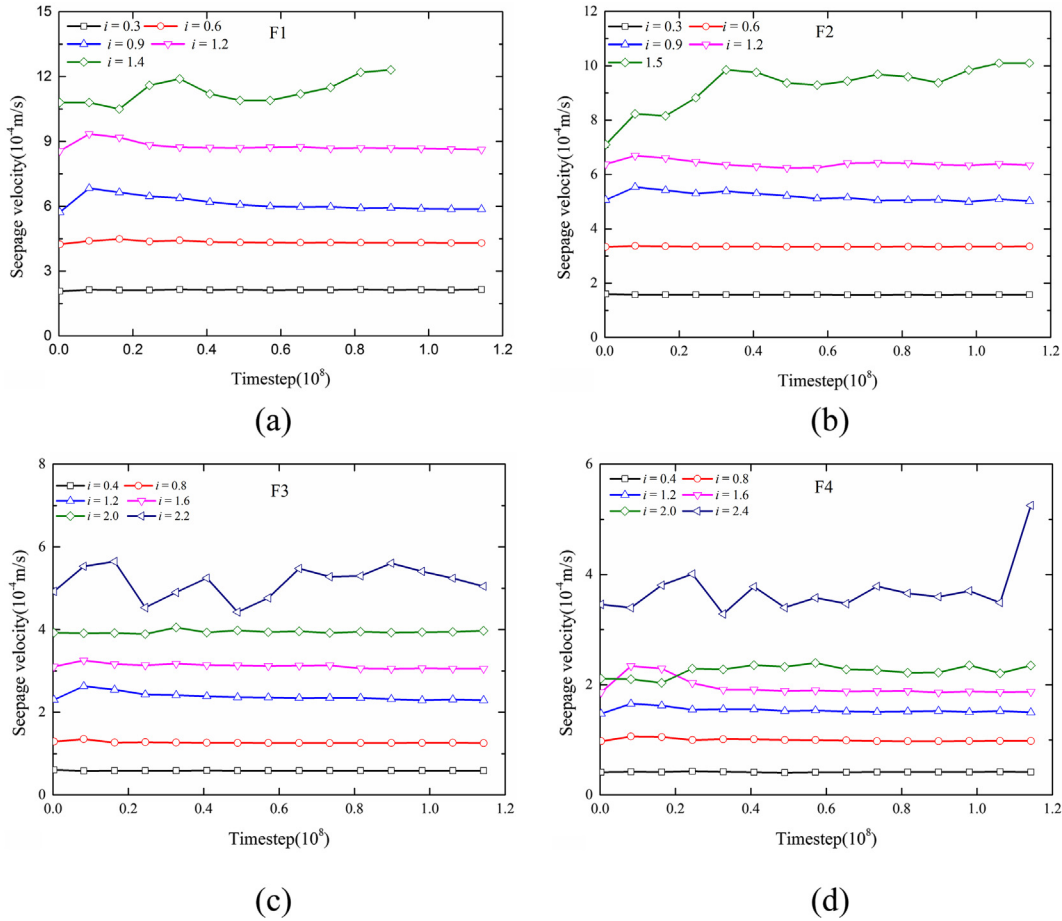


Fig. 9. Superficial velocity v^0 of fine-grained soils.

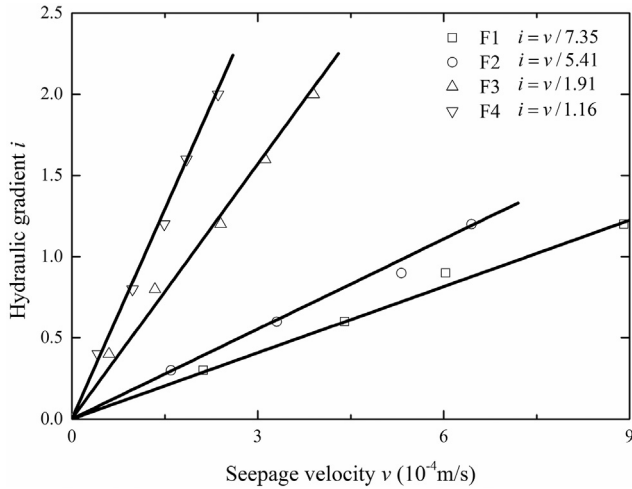


Fig. 10. The relationship $i - v$ of the numerical model for fine-grained soils.

n . Hence, seepage velocity v^0 could not reach a steady value, as shown in Fig. 9.

From the force chain, each line segment denoted the interaction force acting at the centroid of the adjacent particles (Table 5). It was distributed uniformly among all the particles in the initial stage, but it was concentrated on the large particles when $i = 1.2$, owing to the suspension of the small particles in the development stage. At the failure stage, although the suspended particles were adjacent to each other, the contact force almost did not exist, namely, the effective stress was close to zero. Hence, the global seepage failure, i.e., flowing soil,

Table 4

Comparison between the CFD-DEM model and laboratory test results of fine-grained soils.

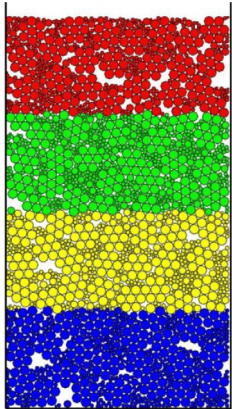
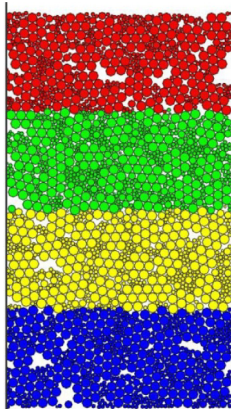
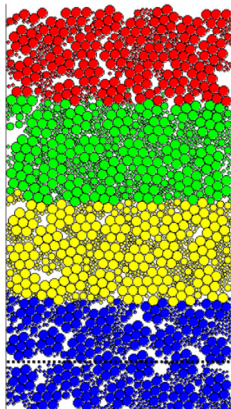
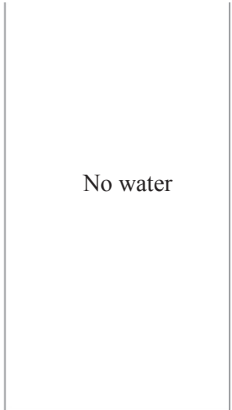
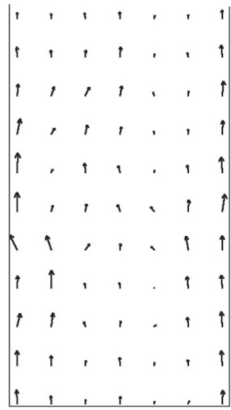
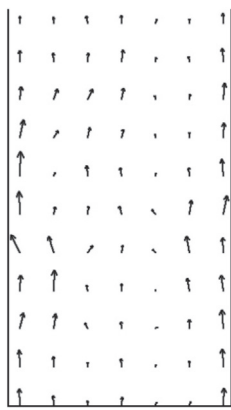
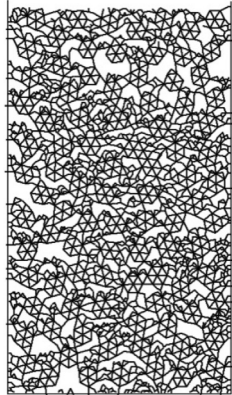
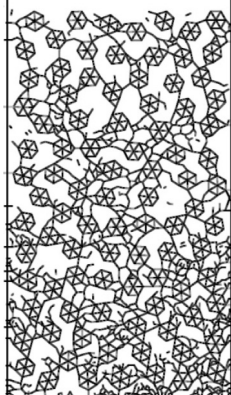
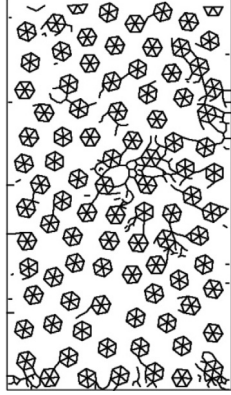
	Numerical modeling			Laboratory test		
	k (10^{-4} m/s)	i_c	R^2	k (10^{-4} m/s)	i_c	R^2
F1	7.35	1.35	0.93	7.11	1.13	0.96
F2	5.41	1.45	0.95	5.83	1.26	0.95
F3	1.91	2.15	0.95	2.07	2.30	0.98
F4	1.16	2.35	0.97	1.03	2.49	0.98

was developed because of the loss of bearing capacity.

From the particle trajectory, nine particles were tracked in the simulation scheme to investigate the particle motion characteristics, as shown in Fig. 11. The particle trajectory in F1 was a short line segment with a length of less than 2 mm. Because of the low seepage velocity, drag force was so low that the particles merely moved upward in the local area. Moreover, the migration distance of the particles between the two side edges was larger than that in the middle zone because of the nonuniform distribution of flow velocity in the seepage field (Table 5).

The term coordination number is defined as the average number of contacts per particle. This number indicates the frequency of collisions and contacts among the particles. The coordination number of F1 gradually decreased with timestep, as shown in Fig. 12. The particle assembly adjusted its position in the local area, and the small particles were gradually suspended, resulting in a decrease in the total number of contacts among the particles. At the critical failure state, all the particles migrated upward at a slow velocity without intermixing or leaping.

Table 5
Seepage failure process of F1.

Stage	Initial stage ($i = 0$)	Development stage ($i = 1.2$)	Failure stage ($i = 1.4$)
Model			
Seepage field	Maximum $v = 0$ 	Maximum $v = 1.08$ mm/s 	Maximum $v = 1.46$ mm/s 
Force chain			

Hence, the coordination number was close to zero.

4.3. Numerical results for coarse-grained soils

The variations in the hydraulic gradient i were 0.02 and 0.2 when i was less than 0.1 and greater than 0.2, respectively. The number of the applied hydraulic gradient of the coarse-grained soils was greater than that of the fine-grained soils because of the nonlinear $i - v$ curve.

4.3.1. Verification of the numerical model

The relationship of $i - v$ obtained in the numerical model is nonlinear, as shown in Fig. 13. This is in accordance with the results obtained in the laboratory tests (Fig. 7). The functional relationship was well conformed to Forchheimer's equation instead of Darcy's law.

Forchheimer's equation is given by the following

$$i = av^2 + bv \tag{7}$$

Compared with the fine-grained soils, the migration rate of pore water was higher, and the Reynolds number was larger (the largest value was 400) in the coarse-grained soils. The pore water could not remain laminar, and thus, it changed to a turbulent flow. The value of drag force of the pore water against the particles was large, mainly dominated by the inertial force mentioned in Eq. (4). Thus, the $i - v$ curve had the shape of a parabola. The drag force coefficient increased with the dry density, which contributed to the enhancement of impermeability.

Piping appeared in specimens C1, C2, C3, and C4, which was identified with the corresponding laboratory tests. The coefficient in

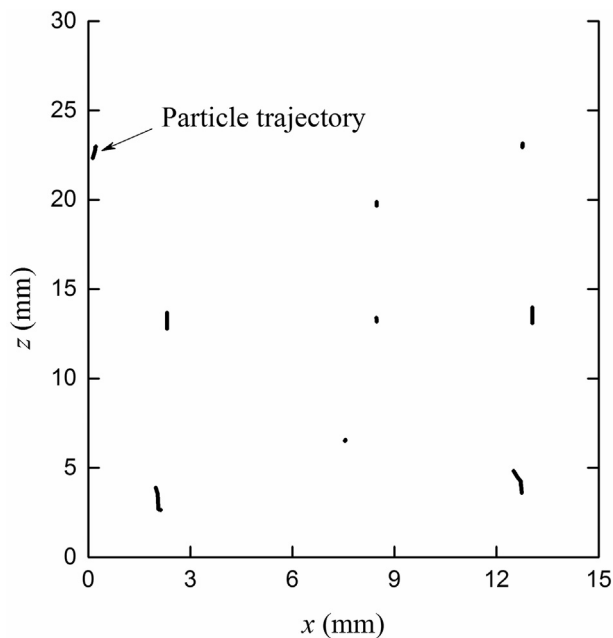


Fig. 11. Particle trajectory in F1.

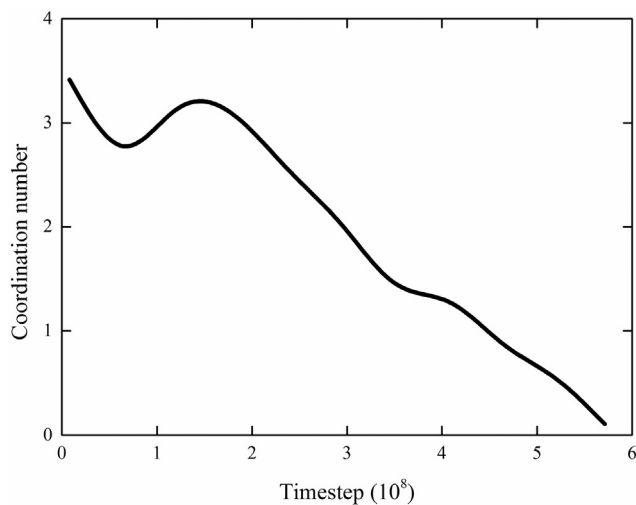


Fig. 12. Coordination number in F1.

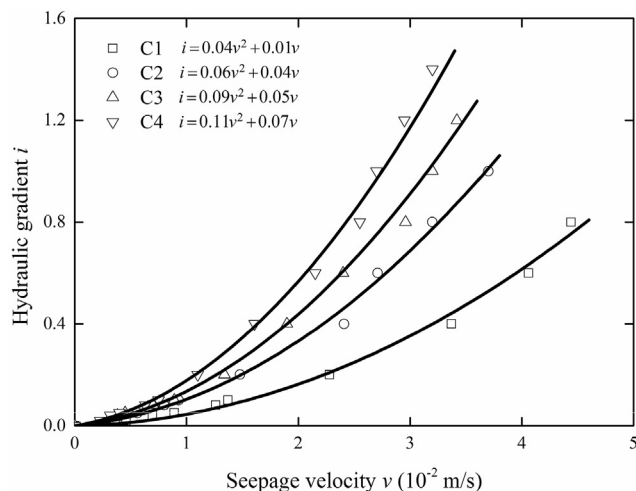


Fig. 13. The relationship $i - v$ of the numerical model for coarse-grained soils.

Table 6

Comparison between the CFD-DEM model and the laboratory test results of coarse-grained soils.

	Numerical modeling			Model experiment		
	$i - v$	i_c	R^2	$i - v$	i_c	R^2
C1	$i = 0.04v^2 + 0.01v$	0.90	0.95	$i = 0.04v^2 + 0.05v$	0.79	0.99
C2	$i = 0.06v^2 + 0.04v$	1.10	0.99	$i = 0.07v^2 + 0.06v$	1.08	0.96
C3	$i = 0.09v^2 + 0.05v$	1.30	0.96	$i = 0.09v^2 + 0.07v$	1.19	0.97
C4	$i = 0.11v^2 + 0.07v$	1.50	0.99	$i = 0.12v^2 + 0.09v$	1.28	0.99

Forchheimers’s equation and the critical gradient listed in Table 6 were close to those obtained from the laboratory tests. These verified the rationality of the application of the CFD-DEM model to investigate the seepage characteristics of coarse-grained soils.

4.3.2. Micro analysis of seepage failure for coarse-grained soils

Like fine-grained soils, typical model diagrams, seepage fields, corresponding force chains, and particle trajectory were recorded to investigate the development process of piping from micro perspective. Taking C1 as an example, the details are discussed as follows.

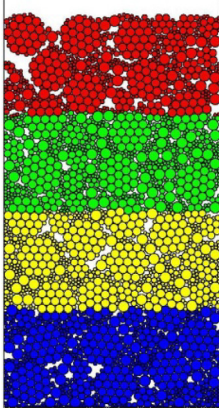
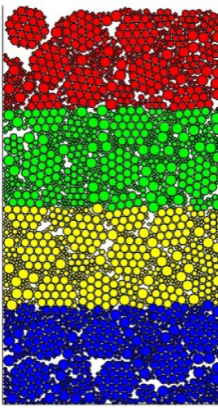
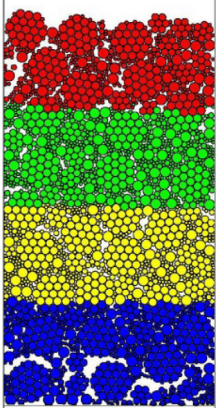
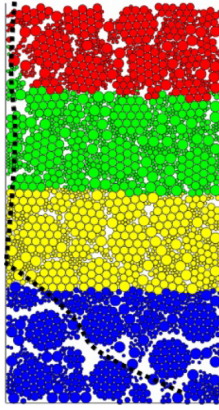
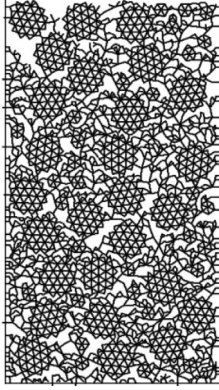
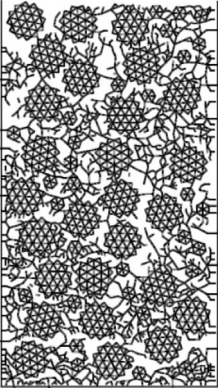
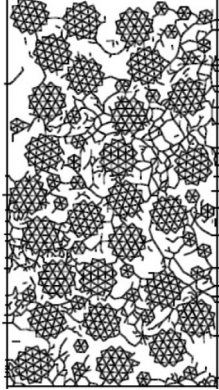
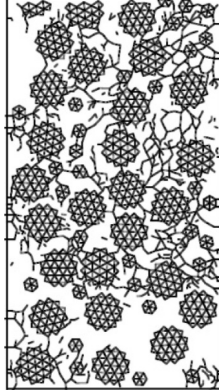
From the model diagram, the particle assembly was uniformly distributed in the initial stage (Table 7). Because of the applied hydraulic gradient i , several local visible holes were enlarged and interconnected with each other owing to the suspension of small particles at the bottom. Then, in the development stage, the small particles at the top left of specimen C1 started to migrate upward and contributed to the floating of a large particle. When the hole at the top left and bottom right of the specimen cut through, an entire pore connectivity area was finally developed and piping failure occurred.

From the seepage field, the development of piping could be observed clearly (Table 7). The seepage field was distributed uniformly in the connection stage. Subsequently, with the increase in i , preferential flow appeared on the top left and bottom right of the specimen, where the small particles were lost. After the seepage duct was formed, the pore water was deflected toward the seepage path. This was significantly different from the observations for fine-grained soils with a near-uniform seepage field.

Force chain was distributed uniformly among all the particles in the initial stage, but it was concentrated mainly on the large particles in the connection stage, which resulted from the disappearance of the contact force in the small particles (Table 7). After an entire seepage duct was formed, the binding effect of the large particles against the small particles was lost, and there was no force chain in the local connected area. Hence, the small particles migrated freely. However, on account of the skeletal support effect of the large particles, the force chain in the other area always existed. There was some effective stress in the coarse-grained soils, and local seepage failure, i.e., piping, was developed. This showed a prominent difference with fine-grained soils where the effective stress was close to zero and global seepage failure i.e., flowing soil, appeared.

From the particle trajectory, the migration distance of the particles in the local connected area was larger than that in the other areas, as shown in Fig. 14. Nevertheless, the cluster particles were surveyed to move a short distance, which was similar to the local re-arrangement of the particle assembly. Compared with the fine-grained soils, the trajectory of the small particles in the coarse-grained soils consisted of long, nonlinear, and stochastic line segments with lengths of several centimeters. Moreover, small particles as a whole moved upward circuitously under the influence of the hydraulic gradient. The small particles in the connectivity area continually floated, bounced, and changed their direction of motion because of obstruction by the large particles. Hence, the local flow regime of the pore water was changed by the porosity variation in the fluid cell because of the wide range of migration of the small particles. In return, the motion characteristics of

Table 7
Seepage failure process of C1.

Stage	Initial stage ($i = 0$)	Connection stage ($i = 0.8$)	Development stage ($i = 1.0$)	Failure stage ($i = 1.0$)
Model				
Seepage field	Maximum $v=0$ No water	Maximum $v=0.12$ m/s	Maximum $v=0.16$ m/s	Maximum $v=0.21$ m/s
Force chain				

the particles were affected by the transformational seepage field. The results revealed that the kinematics and hydraulic features of the system changed dynamically. Thus, their interactive behaviors during the piping were clarified.

5. Conclusions

A coupled CFD-DEM model was applied to simulate the seepage tests on fine-grained and coarse-grained soils (based on material composition in the Tangjiashan landslide dam) with various dry densities. The numerical model was validated with the corresponding laboratory test. The seepage characteristics and seepage failure mechanism were revealed from the macro and micro perspectives. The main results are as follows:

- (1) The calculated seepage parameters, critical hydraulic gradient, and failure mode were in good agreement with the experimental data. The seepage failure modes for fine-grained and coarse-grained soils were flowing soil and piping, respectively.
- (2) The relationship between hydraulic gradient and seepage velocity for the fine-grained soils was conformed to Darcy's law due to the Reynolds number of less than 2. Nevertheless, it was in accordance with Forchheimer's equation for the coarse-grained soils because the migration rate of pore water was higher and the Reynolds number (up to 400) was larger.
- (3) The particle trajectory in the fine-grained soils was a short line segment, and the seepage field was distributed uniformly. The value of seepage velocity increased with the hydraulic gradient, and its direction did not change. At the critical failure state, the entire particle assembly floated upward, and the contact force among

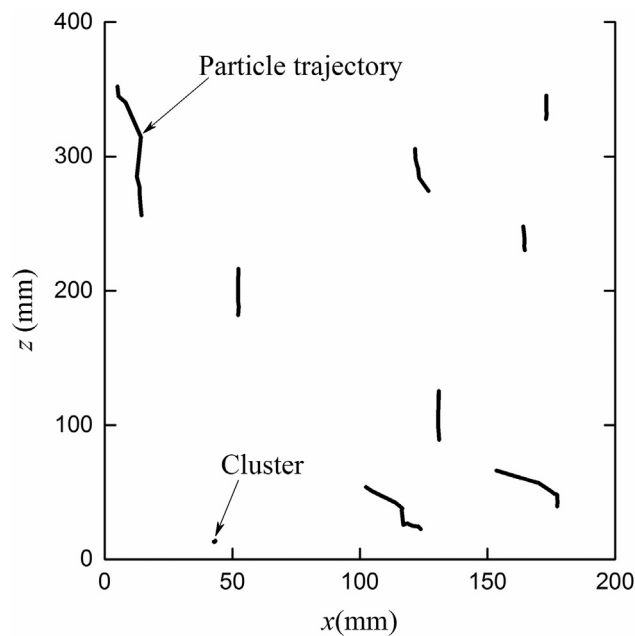


Fig. 14. Particle trajectory in C1.

particles disappeared, which resulted in a global seepage failure, i.e., flowing soil.

- (4) The trajectory of the small particles in the coarse-grained soils was long, nonlinear, and stochastic line segments. The seepage field was gradually deflected with the increase in hydraulic gradient. The preferential flow occurred and contributed to the loss of small particles in the hole. At the critical failure state, an entire pore connectivity area appeared in the specimen; there was some effective stress, and local seepage failure, i.e., piping, occurred. These were dramatically different from the observations for fine-grained soils.

The rationality of the application of the CFD-DEM model to investigate the seepage characteristics of landslide dam materials was verified in this study. Further research should be focused on the Message Passing Interface (MPI) parallelization to speed up the calculation and the process of development of seepage failure in three-dimensional conditions.

Acknowledgements

The research reported in this paper was substantially supported by the Natural Science Foundation of China (No. 41502275 and No. 41731283) and the Shanghai Committee of Science and Technology (No. 14YF1403800).

References

- [1] Korup O. Recent research on landslide dams—a literature review with special attention to New Zealand. *Prog Phys Geogr* 2002;26(2):206–35.
- [2] Stefanelli CT, Segoni S, Casagli N, Catani F. Assessing landslide dams evolution: a methodology review. *Workshop on world landslide forum*. Cham: Springer; 2017. p. 253–7.
- [3] Costa JE, Schuster RL. Documented historical landslide dams from around the world. *US Geological Survey* 1991:91–239.
- [4] Shi Z-M, Ma X-L, Peng M. Statistical analysis and efficient dam burst modelling of landslide dams based on a large-scale database. *Chin J Rock Mech Eng* 2014;33(9):1780–90.
- [5] Huang D, Chen J, Chen L, Wang S. Experimental study of the mechanism of flowing soil for homogeneous cohesionless soil. *Chin J Rock Mech Eng* 2015;34:3424–31.
- [6] Yang K-H, Wang J-Y. Experiment and statistical assessment on piping failures in soils with different gradations. *Mar Georesour Geotechnol* 2017;35(4):512–27.
- [7] Ermini L, Casagli N. Prediction of the behavior of landslide dams using a geomorphological dimensionless index. *Earth Surf Proc Land* 2003;28(1):31–47.
- [8] Shi Z-M, Guan S-G, Peng M, Zhang L-M, Zhu Y, Cai Q-P. Cascading breaching of the Tangjiashan landslide dam and two smaller downstream landslide dams. *Eng Geol* 2015;193:445–58.
- [9] Fan X, Xu Q, Westen CJ-V, Huang R, Tang R. Characteristics and classification of landslide dams associated with the 2008 Wenchuan earthquake. *Geoenviron Disasters* 2017;4(1):12.
- [10] Wang Z-Z, Yang S-P. On characteristics of seepage from earthquake-induced barrier bar of the Xiaonanhai reservoir. *Acta Geol Sichuan* 2003;23(1):26–30.
- [11] Hu X-W, Luo G, Wang J. Seepage stability analysis and dam-breaking mode of Tangjiashan barrier dam. *Chin J Rock Mech Eng* 2010;29(7):1409–17.
- [12] Richards KS, Reddy KR. Critical appraisal of piping phenomena in earth dams. *Bull Eng Geol Environ* 2007;66(4):381–402.
- [13] Shen S-L, Wu H-N, Cui Y-J, Yin Z-Y. Long-term settlement behaviour of metro tunnels in the soft deposits of Shanghai. *Tunn Undergr Space Technol* 2014;40:309–23.
- [14] Shen S-L, Wu Y-X, Misra A. Calculation of head difference at two sides of a cut-off barrier during excavation dewatering. *Comput Geotech* 2017;91:192–202.
- [15] Skempton AW, Brogan JM. Experiments on piping in sandy gravels. *Geotechnique* 1994;44(3):449–60.
- [16] Fontana N. Experimental analysis of heaving phenomena in sandy soils. *J Hydraul Eng* 2008;134(6):794–9.
- [17] Indraratna B, Nguyen VT, Rujikiatkamjorn C. Assessing the potential of internal erosion and suffusion of granular soils. *J Geotech Geoenviron Eng* 2011;137(5):550–4.
- [18] Ke L, Takahashi A. Strength reduction of cohesionless soil due to internal erosion induced by one-dimensional upward seepage flow. *Soils Found* 2012;52(4):698–711.
- [19] Chang D-S, Zhang L-M. Extended internal stability criteria for soils under seepage. *Soils Found* 2013;53(4):569–83.
- [20] Okeke ACU, Wang F. Critical hydraulic gradients for seepage-induced failure of landslide dams. *Geoenviron Disasters* 2016;3(1):9.
- [21] Zhao JD, Tong S. Coupled CFD-DEM simulation of fluid-particle interaction in geomaterials. *Powder Technol* 2013;239(17):248–58.
- [22] Cundall PA, Strack ODL. A discrete numerical mode for granular assemblies. *Geotechnique* 1979;29(1):47–65.
- [23] Muir WD. Modelling mechanical consequences of erosion. *Geotechnique* 2010;60(6):447–57.
- [24] Hicher PY. Modelling the impact of particle removal on granular material behavior. *Geotechnique* 2013;63(2):118–28.
- [25] Suzuki K, Bardet JP, Oda M. Simulation of upward seepage flow in a single column of spheres using discrete-element method with fluid-particle interaction. *J Geotech Geoenviron Eng* 2007;133(1):104–9.
- [26] Chen F, Drumm EC, Guiochon G. Coupled discrete element and finite volume solution of two classical soil mechanics problems. *Comput Geotech* 2011;38(5):638–47.
- [27] Jing L, Kwok CY, Leung YF. Extended CFD-DEM for free-surface flow with multi-size granules. *Int J Numer Anal Meth Geomech* 2015;40(1):62–79.
- [28] Zhao T. “Introduction to the DEM-CFD Coupling Model.” *Coupled DEM-CFD Analyses of Landslide-Induced Debris Flows*. Singapore: Springer; 2017. p. 91–134.
- [29] Anderson TB, Jackson R. Fluid mechanical description of fluidized beds. *Equations of motion*. *Ind Eng Chem Fundam* 1967;6(4):527–39.
- [30] Tsuji Y, Kawaguchi T, Tanaka T. Discrete particle simulation of two-dimensional fluidized bed. *Powder Technol* 1993;77(1):79–87.
- [31] Ergun S. Fluid flow through packed columns. *J Mater Sci Chem Eng* 1952;48(2):89–94.
- [32] Vries JD. Prediction of non-darcy flow in porous media. *J Irrig Drain Div* 1979;105:147–62.
- [33] Sakai M, Takahashi H, Pain CC, Latham JP, Xiang J. Study on a large-scale discrete element model for fine particles in a fluidized bed. *Adv Powder Technol* 2012;23(5):673–81.
- [34] Fan X, Westen CJ-V, Xu Q. Analysis of landslide dams induced by the 2008 Wenchuan earthquake. *J Asian Earth Sci* 2012;57(6):25–37.
- [35] Chang D-S, Zhang L-M, Xu Y. Field testing of erodibility of two landslide dams triggered by the 12 May Wenchuan earthquake. *Landslides* 2011;8(3):321–32.
- [36] Zhao H-F, Zhang L-M, Xu Y. Variability of geotechnical properties of a fresh landslide soil deposit. *Eng Geol* 2013;166(8):1–10.
- [37] Itasca. Fixed coarse-grid fluid scheme in PFC2D. *The PFC2D user’s manual*; 2004.
- [38] SL237-1999. Specification of soil test (in Chinese).
- [39] Li X, Zhao J-D. Numerical simulation of dam break by a coupled CFD-DEM approach. *Jpn Geotech Soc Spec Publ* 2015;2(18):691–6.